Are Adaptive Galerkin Schemes Dissipative?

Rodrigo M Pereira, Natacha Nguyen van Yen, Kai Schneider, Marie Farge

ARE ADAPTIVE GALERKIN SCHEMES DISSIPATIVE?*†

RODRIGO M. PEREIRA ‡, NATACHA NGUYEN VAN YEN §¶, KAI SCHNEIDER ‖, AND MARIE FARGE §

Abstract. Adaptive Galerkin numerical schemes integrate time-dependent partial differential equations with a finite number of basis functions, and a subset of them is selected at each time step. This subset changes over time discontinuously according to the evolution of the solution; therefore the corresponding projection operator is time-dependent and nondifferentiable, and we propose using an integral formulation in time. We analyze the existence and uniqueness of this weak form of adaptive Galerkin schemes and prove that nonsmooth projection operators can introduce energy dissipation, which is a crucial result for adaptive Galerkin schemes. To illustrate this, we study an adaptive Galerkin wavelet scheme which computes the time evolution of the inviscid Burgers equation in one dimension and of the incompressible Euler equations in two and three dimensions with a pseudospectral scheme, together with coherent vorticity simulation which uses wavelet denoising. With the help of the continuous wavelet representation we analyze the time evolution of the solution of the 1D inviscid Burgers equation: We first observe that numerical resonances appear when energy reaches the smallest resolved scale, then they spread in both space and scale until they reach energy equipartition between all basis functions, as thermal noise does. Finally we show how adaptive wavelet schemes denoise and regularize the solution of the Galerkin truncated inviscid equations, and for the inviscid Burgers case wavelet denoising even yields convergence towards the exact dissipative solution, also called entropy solution. These results motivate in particular adaptive wavelet Galerkin schemes for nonlinear hyperbolic conservation laws. This SIGEST article is a revised and extended version of the article [R. M. Pereira, N. Nguyen van yen, K. Schneider and M. Farge, *Multiscale Model. Simul.*, 20 (2022), pp. 1147–1166].

Key words. wavelets, adaptivity, Galerkin method, dissipation

AMS subject classifications. 65N30; 65N50; 65T60; 65M60

DOI. 10.1137/23M1588627

Contents.

*The French Research Federation for Fusion by Magnetic Confinement and the PEPS program of CNRS-INSMI are acknowledged for financial support. NVY thanks the Humboldt foundation for post-doctoral support.

†This work, supported by the European Union under the contract of Association between EURATOM, CEA and the French Research Federation for Fusion by Magnetic Confinement, was carried out within the framework of the European Fusion Development Agreement. The views and opinions expressed herein do not necessarily reflect those of the European Commission.

‡Instituto de Física, Universidade Federal Fluminense, Niterói, Brazil

§LMD–CNRS, École Normale Supérieure-PSL, Paris, France

¶FB Mathematik und Informatik, Freie Universität Berlin, Berlin, Germany

‖Institut de Mathématiques de Marseille (I2M), CNRS, Aix-Marseille Université, Marseille, France

1. Introduction. Since most nonlinear partial differential equations (PDEs) cannot be solved analytically, it is often necessary to use numerical experimentation to explore their approximate solutions with numerical techniques and computers. This can be illustrated in a remark by Bertrand Russel, from 1931: "Although this may seem a paradox, all exact science is dominated by the idea of approximation" [21]. The intrinsic limitations of computers impose that numerical methods for PDEs only solve the truncated system with a finite number of modes, which is designed to closely approach the exact solution. In some cases, however, the truncation has drastic effects that completely destroy the desired approximation. A first historical example for which this happened was probably the symmetric finite-difference scheme designed by von Neumann in the 1940s for nonlinear conservation laws. As recalled in [39], it was indeed shown in the 1980s that when applying von Neumann's scheme, even to the simplest case of the one-dimensional (1D) inviscid Burgers equation, convergence to the correct solution is lost as soon as the first shock appears. Other schemes were then specifically designed to dissipate energy at the location of shocks (see, e.g., [71]), which do not suffer from this limitation and yield the desired solution.

Motivated by achieving high accuracy at reduced computational cost compared to uniform grid methods, numerous adaptive discretization schemes to solve evolutionary PDEs have been developed for decades; see, e.g., [6]. Applied problems, for instance, studying fluid and plasma turbulence, typically involve a multitude of active spatial and temporal scales. To solve them, numerically adaptive schemes concentrate the computational effort at locations and time instants where it is necessary to ensure a given numerical accuracy, whereas elsewhere efforts can be significantly reduced. Among them, multiresolution and wavelet-based methods offer an attractive possibility to introduce locally refined grids, which dynamically track the evolution of the solution in space and scale. Examples for the 1D Burgers equation can be found in [47], reaction-diffusion equations in [32, 34], Stokes equations in [12, 13], and Navier–Stokes equations in [33, 35]. Automatic error control of the adaptive discretization with respect to a uniform grid solution is hereby an advantageous feature [10]. For a review of adaptive wavelet methods in the context of computational fluid dynamics, we refer the reader to [67].

In many applications, in particular in computational fluid dynamics, Galerkin truncated discretizations of PDEs with a finite number of modes are the methods of choice. Spectral methods [60, 7, 63] are a prominent example, and Fourier–Galerkin schemes are widely used for direct numerical simulation of turbulence [40] due to their high accuracy. Today state-of-the-art direct numerical simulations of the incompressible three-dimensional (3D) Navier–Stokes equations currently use up to 6 trillion grid points [74]. For efficiency reasons the convolution product in spectral space, due to the nonlinear quadratic term which is typically encountered in hydrodynamic equations, is evaluated in physical space and aliasing errors are completely removed. This implementation, called pseudospectral formulation with full dealiasing using the 2/3 rule, is equivalent to a Fourier–Galerkin scheme up to round-off errors of the computer [60, 7, 63]. Thus the discretization conserves the L^2-norm of the solution. A classical test to check the stability of pseudospectral codes, e.g., for viscous Burgers or Navier–Stokes equations, is to perform simulations with zero viscosity. This allows one to verify if the L^2-norm of the solution, i.e., typically energy, is conserved and given that time steps are sufficiently small, the truncated Galerkin schemes are stable. However, after some time the solution of the Galerkin truncated inviscid equations, e.g., inviscid Burgers or incompressible Euler, develops a peculiar behavior when localized oscillations appear due to numerical resonances and spread in space and wavenumber as a white noise, a behavior leading to energy equipartition between all Fourier coefficients known as thermalization. This energy equipartition had already been predicted in 1952 by T.D. Lee [45] for spectral approximations of 3D incompressible Euler by applying Liouville's theorem from statistical mechanics.

The effect of truncating Fourier–Galerkin schemes was studied in [48] for the 1D Burgers equation and in [8] for the 3D incompressible Euler equation. Detailed numerical studies were carried out for the 1D Burgers equation [65], where high-wavenumber oscillations were observed and interpreted as first manifestations of thermalization [45]. We also refer the reader to the discussion on the statistical equilibrium in two-dimensional (2D) turbulence using the truncated Euler equations by Kraichnan [44]. In [50] it was then proposed that those oscillations may be eliminated by canceling a few Fourier modes in a narrow band next to the cut-off (Nyquist) wavenumber. In [64] early time numerical resonances and singularities in the inviscid Burgers equation were analyzed. In [18] it was shown for 1D Burgers that the process of thermalization first takes place in well-defined subdomains, before filling the whole space.In [51] further studies for the 3D incompressible Euler equation were performed and the seeds of thermalization were modeled as an effective 1D problem. In [43] a study of the 3D axisymmetric Galerkin truncated incompressible Euler equations was performed and potentially singular solution were examined showing likewise the presence of oscillatory structures.

Motivated by [65, 61], a detailed numerical analysis of Fourier–Galerkin methods for nonlinear evolutionary PDEs was performed in [4], proving spectral convergence for smooth solutions of the inviscid Burgers equation and the incompressible Euler equations. However, when the solution lacks sufficient smoothness, then both the spectral and pseudospectral Fourier methods with 2/3 dealiasing exhibit nonlinear instabilities which generate high-wavenumber oscillations. In particular it was shown that after the shock formation in the inviscid Burgers equation, the total variation of bounded (pseudo)spectral Fourier solutions must increase with the number of modes. The L^2-energy conservation of the spectral

solution is reflected through high-wavenumber oscillations, which is in contrast with energy dissipating Onsager solutions [56]. Onsager conjectured the existence of dissipative solutions with any Hölder exponent smaller than 1/3 [11, 15].

These issues are closely related to what is known in the turbulence literature as the dissipative anomaly. This refers to the fact that time reversal symmetry is not restored in the limit where the symmetry breaking parameter, i.e., viscosity, goes to zero. To reproduce the expected dissipative behavior in truncated Galerkin approximations, these numerical resonances must be removed. For this purpose different numerical regularization techniques have been proposed, which are commonly used in numerical methods for solving hyperbolic conservation laws. If the solution is not unique, the regularized numerical scheme selects one weak solution, which should correspond to the physically relevant one, e.g., the entropy solution of the inviscid Burgers equation, which can be computed exactly using the Legendre transform [73]. These approaches include upwind techniques [58], total variation diminishing schemes [38], shock limiters [71], spectral vanishing viscosity [72, 36], inviscid regularization schemes [3, 41], and classical viscosity and hyperviscosity [5]. In the case of hyperviscosity, it has been shown [30, 2] that for sufficiently high powers of the Laplacian in the dissipative term, the unregularized conservative dynamics is recovered, while for moderate powers a bottleneck effect occurs in the energy spectrum [31], i.e., a bump in the spectrum between the inertial and dissipation ranges. As mentioned above, a method based on the suppression of a narrow band of Fourier modes at discrete time intervals was recently proposed in [50], and the resulting solution exhibits numerical convergence to the entropy solution as the spatial resolution increases. This method, which has almost no additional computational cost, can be viewed as a periodic filtering in Fourier space, where the Galerkin projection space changes discontinuously at regular time intervals. These discontinuous changes in the projection operators are precisely the type of situation we intended to formalize in [62] and in the present paper, but on more general grounds, taking into account other possible projection bases.

In the context of adaptive wavelet schemes, numerical experiments with the 1D inviscid Burgers equation showed that wavelet filtering of the Fourier–Galerkin truncated solution in each time step, which corresponds to denoising and which removes the numerical resonances, yields the solution to the viscous Burgers equation [52, 61]. For the 2D incompressible Euler equations [53, 61] different wavelet techniques for regularizing truncated Fourier–Galerkin solutions were studied using either real-valued or complex-valued wavelets, and the results were compared with viscous and hyperviscous regularization methods. The results show that nonlinear wavelet filtering with complex-valued wavelets preserves the flow dynamics and suggests L^2 convergence to the reference solution. The wavelet representation offers at the same time a nonnegligible compression rate of about 3 for fully developed 2D turbulence [27, 68].

Simulations of the 3D wavelet-filtered Navier-Stokes equations [55] showed that statistical predictability of isotropic turbulence can be preserved with a reduced number of degrees of freedom. This approach, called coherent vorticity simulation (CVS) [27, 25], is a multiscale method to compute incompressible turbulent flows using wavelet-based denoising of the vorticity field at each time step. The coherent vorticity, corresponding to the few wavelet coefficients whose modulus is larger than a threshold, represents the organized and energetic flow part, while the remaining incoherent vorticity induces a velocity field which is

similar to a Gaussian white noise and corresponds to thermalization [24]. Applications to different canonical turbulent flows can be found in [24, 28, 66, 54], including MHD and plasma turbulence [26]. Applying wavelet-based denoising to the 3D Galerkin truncated incompressible Euler equations confirmed that this adaptive regularization models turbulent dissipation and thus allows one to compute turbulent flows which exhibit intermittent nonlinear dynamics and a $k^{-5/3}$ Kolmogorov energy spectrum [23]. A significant compression rate of the wavelet coefficients of vorticity is likewise observed which reduces the number of active degrees of freedom to be computed.

The aim of the current work is to provide a mathematical framework to analyze the properties of evolutionary PDEs discretized with adaptive Galerkin schemes. Galerkin schemes are particularly appealing due to their optimality properties, regarding best approximation in the energy norm, conservation of energy, and the ease of numerical analysis using Hilbert space techniques. Introducing space adaptivity, such as a wavelet filtering in each time step, implies that the projection operator changes over time as only a subset of basis functions is used. Hence, the projection operator is nondifferentiable in time and we propose the use of an integral formulation. The projected equations are then analyzed with respect to existence and uniqueness of the solution. It is proven that nonsmooth projection operators introduce dissipation, a result which is crucial for adaptive discretizations of nonlinear PDEs. Existence and uniqueness of the solution of the projected equations is likewise shown. Tools from countable systems of ordinary differential equations (ODEs) and functional analysis in Banach spaces are used. For related background we refer the reader to the textbooks [16, 69] and [29].

The outline of the article is as follows. First the mathematical framework of adaptive Galerkin schemes is defined in section 2, and the existence and uniqueness of the projected equations is analyzed, providing an explanation to the energy dissipation. Space and time discretizations of the Burgers and incompressible Euler equations are described in section 3, presenting likewise wavelet denoising and the coherent vorticity simulation method. Numerical examples in section 4 in which a single coefficient is discarded illustrate the dissipation mechanism. Section 5 analyzes in both space and scale how numerical resonances appear and develop in the solution of the Fourier-truncated 1D inviscid Burgers equation by using complex-valued wavelets, which are continuously dilated and translated. It is then shown how wavelet denoising removes those numerical resonances in the 1D inviscid Burgers equation and the 2D and 3D incompressible Euler equations. A conclusion is drawn in section 6.

2. Adaptive Galerkin schemes. Evolutionary PDEs can be discretized with a Galerkin method in space by projecting the equation onto a sequence of finite-dimensional linear spaces, which approximate the solution in space when the discretization parameter, h, goes to zero. Using truncation to a finite number of modes, the infinite-dimensional countable system of ODEs in time can be reduced. An important restriction of such methods is that the projection space typically does not evolve in time and the number of modes is fixed. Here, we propose a formulation of adaptive Galerkin discretizations where the projection operator and the number of modes can change over time, and we show that, under suitable conditions, adaptation can introduce dissipation.

2.1. Galerkin projection. Let H be a Banach space, and consider the evolution equation

$$u' = f(u), \tag{2.1}$$

where u' denotes the weak time derivative of u and f is defined and continuous from some sub-Banach space $D(f) \subset H$ into H. Equation (2.1) is completed by a suitable initial condition $u(0) = u(t = 0)$. To be more specific, we shall focus below on the case of the 1D Burgers equation on the torus $\mathbb{R}/\mathbb{Z}$,

$$\partial_t u + u\partial_x u = \nu \partial_{xx} u, \tag{2.2}$$

which corresponds to (2.1) with

$$f(u) = \nu \partial_{xx} u - u\partial_x u \tag{2.3}$$

and $u = u(x, t)$.

The classical Galerkin discretization of (2.1) is defined as follows: for $h > 0$, let H_h be a fixed finite-dimensional subspace of $D(f)$, such that

$$\overline{\bigcup_{h>0} H_h} = H,$$

where the adherence is taken in H, and let P_h be the orthogonal projector on H_h. Find $u_h : [0, T] \in H_h$ such that

$$u'_h = P_h f(u_h) = P_h(\nu \partial_{xx} u_h - u_h \partial_x u_h). \tag{2.4}$$

Now for $t \in [0, T]$, assume that $P_h(t)$ is an orthogonal projector on some finite-dimensional subspace $H_h(t)$ of H. The dimension of $H_h(t)$ is allowed to change in time, but we assume that $H_h(t)$ remains within a fixed finite-dimensional subspace H_h^0. P_h therefore takes its values in the set of orthogonal projectors $H_h^0 \to H_h^0$, which we denote by Π_h^0, with its natural smooth manifold structure as a closed subset of all linear mappings $H_h^0 \to H_h^0$. We want to find $u_h : [0, T] \in H_h(t)$, which is an approximation of u.

2.2. Time-dependent Galerkin schemes. Let us first assume that P_h is a smooth function of time. As in the case where P_h is time independent, we apply $P_h(t)$ to the differential equation to get

$$P_h(t)u'_h(t) = P_h(t)f(u_h(t)), \tag{2.5}$$

but now, since P_h does not commute with the time derivative, this equation is not sufficient to determine $u'_h(t)$ entirely. We need another equation to fix the component of $u'_h(t)$ which is in the orthogonal of $H_h(t)$, i.e., in $H_h^\perp(t)$.

To derive this equation, we start from the condition that $u_h(t) \in H_h(t)$ for every t, which is equivalent to

$$P_h(t)u_h(t) = u_h(t). \tag{2.6}$$

Differentiating this identity in time leads to

$$P_h(t)u'_h(t) + P'_h(t)u_h = u'_h(t), \tag{2.7}$$

or equivalently

$$(1 - P_h(t))\, u_h'(t) = P_h'(t) u_h(t), \tag{2.8}$$

which is precisely the equation we were looking for. By adding (2.5) and (2.8) together, we obtain the definition of the adaptive Galerkin scheme:

$$u_h'(t) = P_h(t) f\left(u_h(t)\right) + P_h'(t) u_h(t). \tag{2.9}$$

By comparing this differential equation with (2.4), we observe the appearance of a new term proportional to the time derivative of P_h. This is the essential ingredient which characterizes the adaptive Galerkin scheme. We now show the following.

LEMMA 2.1. *Any solution of (2.9) such that $u_h(0) \in H_h(0)$ also satisfies $u_h(t) \in H_h(t)$ for all t, and moreover*

$$\frac{1}{2}\frac{\mathrm{d}}{\mathrm{d}t}\|u_h(t)\|^2 = (u_h(t), f(u_h(t))). \tag{2.10}$$

Proof. By differentiating $P_h(t)^2 = P_h(t)$ and $P_h(t)^3 = P_h(t)$, respectively, we obtain the identities

$$P_h(t)P_h(t)' + P_h(t)'P_h(t) = P_h(t)' \quad \text{and} \quad P_h(t)P_h(t)'P_h(t) = 0,$$

which imply that

$$\frac{\mathrm{d}}{\mathrm{d}t}\left[(1 - P_h(t))u_h(t)\right] = 0, \tag{2.11}$$

and the first part follows. To prove the second part, take the inner product of the equation with u_h:

$$\frac{1}{2}\frac{\mathrm{d}}{\mathrm{d}t}\|u_h(t)\|^2 = (u_h(t), f(u_h(t))) + (u_h(t), P_h'(t)u_h(t)), \tag{2.12}$$

where the last term can be rewritten as

$$(P_h(t)u_h(t), P_h'(t)P_h(t)u_h(t)) = (u_h(t), P_h(t)P_h'(t)P_h(t)u_h(t)) = 0,$$

which proves (2.10). ∎

2.3. Nonsmooth time-dependent Galerkin schemes. The above computations are valid when P_h is differentiable. This is a severe restriction preventing us in particular from switching on and off dynamically some functions in the basis of integration, which is the goal that we had set ourselves in the beginning, i.e., adaptive Galerkin schemes where basis functions are selected with respect to an adaption criterion at discrete time steps. To proceed we therefore need to extend the definition of the scheme to nondifferentiable P_h. For this we consider the integral formulation of (2.9), namely,

$$u_h(t) = u_h(0) + \int_0^t P_h(\tau) f(u_h(\tau))\mathrm{d}\tau + \int_0^t P_h'(\tau) u_h(\tau)\mathrm{d}\tau. \tag{2.13}$$

This equation can be rewritten using a Stieltjes integral with respect to P_h:

$$u_h(t) = u_h(0) + \int_0^t P_h(\tau) f(u_h(\tau)) \mathrm{d}\tau + \int_0^t \mathrm{d}P_h(\tau) u_h(\tau), \tag{2.14}$$

which we call the integral formulation of the adaptive Galerkin scheme.

This equation makes sense as soon as P_h has bounded variation (BV), which gives it a much wider range of applicability than (2.9), allowing in particular discontinuities in P_h. To solve such an equation we need to resort to the theory of generalized ODEs, which we now recall.

The rigorous setting for integral equations such as (2.14) involving Stieltjes integrals is explained in detail in the book [69]. An alternative introduction can be found in [59]. We summarize the main consequences of the theory for our problem in the following.

THEOREM 2.2. *Assume that $P_h(t) : [0,T] \to$ is of bounded variation and left-continuous, that $P_h(0)u_h(0) = u_h(0)$ (i.e., $u_h(0) \in H_h(0)$), and that $f : H_h^0 \to H$ is locally Lipschitz. Then*

(i) there exists T^*, $0 < T^* \leq T$, such that the integral equation

$$u_h(t) = u_h(0) + \int_0^t P_h(\tau) f(u_h(\tau)) \mathrm{d}\tau + \int_0^t \mathrm{d}P_h(\tau) u_h(\tau) \tag{2.15}$$

has a unique BV, left-continuous solution $u_h : [0,T^*] \to H_h^0$;

(ii) this solution satisfies

$$\forall t \in [0,T], P_h(t)u_h(t) = u_h(t); \tag{2.16}$$

(iii) u_h is continuous at any point of continuity of P_h, and more generally for any t:

$$u_h(t^+) - u_h(t) = \left[P_h(t^+) - P_h(t)\right] u_h(t), \tag{2.17}$$

or equivalently

$$u_h(t^+) = P_h(t^+) u_h(t); \tag{2.18}$$

(iv) the energy equation (2.10) for smooth P_h is replaced in general by

$$\begin{aligned} &\frac{1}{2}(\|u_h(t)\|^2 - \|u_h(0)\|^2) \\ &\quad = \int_0^t (u_h(\tau), f(u_h(\tau)))\mathrm{d}\tau - \frac{1}{2} \sum_{\{i|t_i<t\}} \| \left[(1 - P_h(t_i^+)\right] u_h(t_i)\|^2, \end{aligned} \tag{2.19}$$

where $(t_i)_{i\in\mathbb{N}}$ are the points of discontinuity of P_h.

Proof. To prove part (i) of the theorem we first need to familiarize ourselves with a few key concepts used by [69].

DEFINITION 2.3. *Let $G = \{x \in \mathbb{R}^n \mid \|x\| \leq c\} \times [0,T]$, let $h : [0,T] \to \mathbb{R}$ be a nondecreasing, continuous from the left function, and let $\omega : [0,+\infty) \to \mathbb{R}$ a continuous, increasing function with $\omega(0) = 0$.*

We will say that a function $F : G \to \mathbb{R}^n$ belongs to the class $\mathcal{F}(G, h, \omega)$ if and only if

$$\|F(x, t_2) - F(x, t_1)\| \le |h(t_2) - h(t_1)| \tag{2.20}$$

and

$$\|F(x, t_2) - F(x, t_1) - F(y, t_2) + F(y, t_1)\| \le \omega(\|x - y\|)|h(t_2) - h(t_1)| \tag{2.21}$$

for all $(x, t_2), (x, t_1), (y, t_2), (y, t_1) \in G$.

The proof of the existence is based on the Schauder–Tichonov fixed point theorem, using [69, p. 114, Theorem 4.2]. The uniqueness can be shown using [69, page 122, Theorem 4.8] proving the local uniqueness property in the future, i.e., for increasing t.

Now let us turn to (ii). The idea is to approximate P_h by a family of smooth functions $P_{h,\varepsilon}$, $\varepsilon > 0$, and then to apply Lemma 2.1 to the corresponding solution $u_{h,\varepsilon}$, giving

$$[1 - P_{h,\varepsilon}(t)]\, u_{h,\varepsilon}(t) = 0 \tag{2.22}$$

and then passing to the limit. For this we need $u_{h,\varepsilon}(t) \to u_h(t)$, which means that the solution depends continuously on P_h (see chapter 8," Continuous Dependence on Parameters" [69, p. 262]).

The continuity of u_h in part (iii) follows directly from the fact that P_h is left-continuous and BV.

The energy equation in part (iv) can be shown by integrating (2.12) in time and replacing $P_h'(t)u_h(t)$ by $[1 - P_h(t)]\, u_h'(t)$; cf. (2.8). ∎

In the case when the projector $P_h(t)$ depends on $u(t)$, e.g., when using adaptive wavelet thresholding, we have

$$u_h(t) = u_h(0) + \int_0^t P_h(\tau) f(u_h(\tau)) \mathrm{d}\tau + \int_0^t \mathrm{d}P_h(\tau) u_h(\tau), \tag{2.23a}$$

$$P_h(t) = \Phi(u_h(t)), \tag{2.23b}$$

where Φ is a given function depending on the projected solution u_h.

Conjecture 1. *Under certain conditions the system (2.23) has a unique solution.*

Proof. A possible proof of this conjecture may proceed by iteration. Let P_h^0 be the projector on the time-independent approximation space H_h^0, and let u_h^0 be the corresponding solution of (2.23a). We then define recursively

$$P_h^{n+1}(t) = \Phi(u_h^n(t)) \tag{2.24}$$

and u_h^{n+1} as the solution of (2.23a) with $P_h = P_h^{n+1}$. ∎

3. Numerical discretization applied to the inviscid Burgers and the incompressible Euler equations. Supposing space and time separation, we first apply a Galerkin discretization in space and obtain a finite number of ODEs. Then explicit time discretization is applied for time integration. In addition we present wavelet-based denoising and CVS which is founded on wavelet filtering.

3.1. Space discretization. For space discretization in the numerical results below we use a classical Fourier pseudospectral scheme [60, 7, 63], where the spatial derivatives are computed in spectral space, while the nonlinear term is evaluated in physical space. For quadratic nonlinearities this avoids the computation of costly convolution products in spectral space. The drawback of this method are aliasing errors, which can be removed at the price of increasing the number of computed modes. The spectral Fourier projection of $u \in L^1(\mathbb{T}^d)$ where $\mathbb{T} = \mathbb{R}/(2\pi\mathbb{Z})$ is given by

$$P_N u(\boldsymbol{x}) = u_N(\boldsymbol{x}) = \sum_{|\boldsymbol{k}|\lesssim N/2} \widehat{u}_k \, e^{i\boldsymbol{k}\cdot\boldsymbol{x}} \ , \ \widehat{u}_{\boldsymbol{k}} = \frac{1}{(2\pi)^d} \int_{\mathbb{T}^d} u(\boldsymbol{x}) \, e^{-i\boldsymbol{k}\cdot\boldsymbol{x}} \, d\boldsymbol{x}. \tag{3.1}$$

Note that $|k| \lesssim N/2$ is understood in the sense $-N/2 \leq k < N/2$ and correspondingly in higher dimensions for each component of $\boldsymbol{k}$.

Applying the spectral discretization to the 1D inviscid Burgers equation ($d = 1$),

$$\partial_t u + \frac{1}{2}\partial_x u^2 \ = \ 0 \quad \text{for} \quad x \in \mathbb{T} \quad \text{and} \quad t > 0 \tag{3.2}$$

with periodic boundary conditions and suitable initial condition $u(x, t = 0) = u_0(x)$, yields the Galerkin scheme

$$\partial_t u_N + \frac{1}{2}\partial_x \left(P_N (u_N)^2\right) \ = \ 0 \quad \text{for} \quad x \in \mathbb{T} \quad \text{and} \quad t > 0, \tag{3.3}$$

which corresponds to a nonlinear system of N coupled ODEs for $\widehat{u}_k(t)$ with $|k| \lesssim N/2$. A pseudospectral evaluation of the nonlinear term is utilized, and the product in physical space is fully dealiased. In other words, the Fourier modes retained in the expansion of the solution are such that $|k| \leq k_C$, where k_C is the desired cut-off wavenumber, but the grid has $N = 3k_C$ points in each direction, versus $N = 2k_C$ for a nondealiased, critically sampled product. This dealiasing makes the pseudospectral scheme equivalent to a Fourier–Galerkin scheme up to round-off errors [60, 7, 63], and is thus conservative.

For the 2D and 3D incompressible Euler equations ($d = 2, 3$) with periodic boundary conditions,

$$\begin{aligned} \partial_t \boldsymbol{u} + (\boldsymbol{u}\cdot\nabla)\,\boldsymbol{u} \ &= \ -\nabla p \quad \text{for} \quad \boldsymbol{x} \in \mathbb{T}^d \quad \text{and} \quad t > 0, \\ \nabla \cdot \boldsymbol{u} &= 0, \end{aligned} \tag{3.4}$$

a similar spectral discretization can be applied. The pressure p is eliminated using the Leray projection onto divergence-free vector fields. Eventually a nonlinear system of coupled ODEs is obtained for the Fourier coefficients of the velocity $\widehat{\boldsymbol{u}}_{\boldsymbol{k}}(t)$. Similarly to the Burgers equation, the nonlinear term is evaluated with a pseudospectral method and aliasing errors are completely removed.

3.2. Time discretization. For time discretization of the resulting ODE systems we use classical explicit Runge–Kutta schemes, of order 4 for the 1D Burgers equation and the 3D Euler equations. For 2D Euler, third order Runge–Kutta with a low storage formulation is used; see [57]. For details on the convergence and stability of the above spectral schemes we refer the reader to [4]. Implementation features for the 1D Burgers equation and the 2D Euler equation can be found in [53] and [61]. For details on the scheme for 3D Euler we refer the reader to [23].

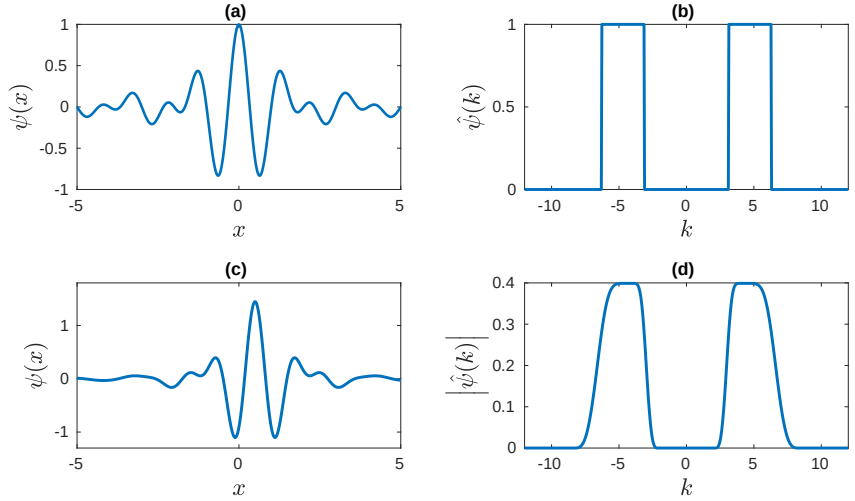

FIG. 1. *Shannon wavelet (top) and Meyer wavelet (bottom) in physical space $\psi(x)$ (left) and the corresponding modulus of the Fourier transform $|\widehat{\psi}(k)|$ (right).*

3.3. Wavelet denoising and Coherent Vorticity Simulation. The Fourier space discretization described above could be replaced by any other Galerkin discretization, using, for instance, finite elements, or wavelets as basis functions. The interest of using wavelets is to introduce adaptive discretizations; see, e.g., [67, 20]. In this case the projector P is changing over time and is nonsmooth, which means that dissipation is introduced by removing/adding basis functions during the time stepping. This technique has been previously used for regularizing the Burgers equation and the incompressible Euler equations without a rigorous mathematical justification [61].

In the following we describe the orthogonal wavelet representation and test the influence of wavelet thresholding for denoising. Therewith we introduce the concept of pseudoadaptive simulations. The Fourier–Galerkin discretization is still used to solve the PDE, but in each time step the numerical solution u_N is decomposed into a periodic orthogonal wavelet series of $L^2(\mathbb{T}^d)$. For $d = 1$ we thus have the 1D truncated wavelet series

$$P_J u_N(x) = u_N^J(x) = \overline{u}_{00} + \sum_{j=0}^{J-1} \sum_{i=0}^{2^j-1} \widetilde{u}_{ji} \psi_{ji}(x)\,, \quad \widetilde{u}_{ji} = \int_{\mathbb{T}} u_N(x)\psi_{ji}(x)dx, \tag{3.5}$$

where $\overline{u}_{00}$ is the mean value of the solution and the $\widetilde{u}_{ji}$ are its wavelet coefficients. The wavelet $\psi_{ji}(x) = 2^{j/2}\psi(2^j x - i)$ quantifies fluctuations at scale 2^{-j} around position $i/2^j$ and $N = 2^J$ denotes the total number of grid points, corresponding to the finest resolution. Figure 1 illustrates Shannon and Meyer wavelets which are not compactly supported, together with the corresponding Fourier transforms which have compact support. This implies that both are trigonometric polynomials and can be spanned by a Fourier basis. For extension to higher dimensions using tensor product construction of wavelets, we refer the reader to [14]. From a computational point of view the additional cost of wavelet thresholding is negligible, as the fast wavelet transform has only $O(N)$ complexity, compared to $O(N \log N)$ for the fast Fourier transform used in the pseudospectral schemes.

Wavelet denoising is the basis of the coherent vorticity simulation (CVS) method designed in 1999 to solve the Navier–Stokes equations [27, 25]. It introduces a sparse representation of the solution by removing the weak wavelet coefficients corresponding to Gaussian white noise. It is based on the idea that Donoho and Johnstone proposed in 1994 for denoising signals corrupted with Gaussian white noise via wavelet shrinkage [19]. Thresholding on the wavelet coefficients with a threshold depending on the variance of the noise is performed at each time step. This yields a projection of the numerical solution u_N,

$$P_J^\epsilon u_N(x) = u_\epsilon^J(x) = \overline{u}_{00} + \sum_{j=0}^{J-1} \sum_{i=0}^{2^j-1} \rho_\epsilon\left(\widetilde{u}_{ji}\right) \psi_{ji}(x), \tag{3.6}$$

where ϵ is the threshold and ρ_ϵ is the (hard) thresholding operator defined as

$$\rho_\epsilon(x) = \begin{cases} x & \text{for} \quad |x| > \epsilon, \\ 0 & \text{for} \quad |x| \leq \epsilon. \end{cases} \tag{3.7}$$

The thresholding error can be estimated (see, e.g., [10]), and we have

$$||P_J u_N(x) - P_J^\epsilon u_N(x)||_2 \leq C\epsilon\,.$$

Using pseudoadaptive simulations the CVS algorithm can be summarized as follows [61]:

i) The Fourier coefficients of the solution $\widehat{u}_k$ for $|k| \lesssim N/2$ are advanced in time to $t = t_{n+1}$ and an inverse Fourier transform is applied on a grid of size N to obtain u_N.
ii) A forward wavelet transform is performed to obtain $P_J u_N(x)$, according to equation (3.5).
iii) CVS filtering removes wavelet coefficients having magnitude below the threshold ϵ. The threshold value is determined iteratively [1] and initialized with $\epsilon_0 = q\sqrt{||u||_2^2/N}$, where q is a compression parameter. The iteration steps are then obtained by $\epsilon_{s+1} = q\sigma[\widetilde{u}_{ji}^s]$ until $\epsilon_{s+1} = \epsilon_s$, where $\widetilde{u}_{ji}^s$ are the wavelet coefficients below ϵ_s and $\sigma[\cdot]$ is the standard deviation of the set of these coefficients.
iv) A safety zone is added in wavelet space to track the solution in space and scale. The index set of retained wavelet coefficients in step (iii) is denoted by Λ, and for each retained wavelet coefficient indexed by $(j,i) \in \Lambda$, neighboring coefficients in position and scale (5 in the present case) are added, as illustrated in Figure 2.
v) An inverse wavelet transform is applied to the wavelet coefficients above the final threshold and a Fourier transform is then performed to obtain the Fourier coefficients of the filtered solution at time step t_{n+1}.

The value of the compression parameter q in the CVS algorithm (iii) controls the number of discarded coefficients, and in previous studies [61] we found experimentally the value $q = 5$ for Kingslets (complex-valued wavelets) and $q = 8$ for orthogonal real wavelets.

Various choices of wavelet basis for regularizing the solution of the Galerkin-truncated inviscid equations have been tested, e.g., in [61], including several orthogonal wavelet bases as well as the dual-tree complex wavelet basis introduced

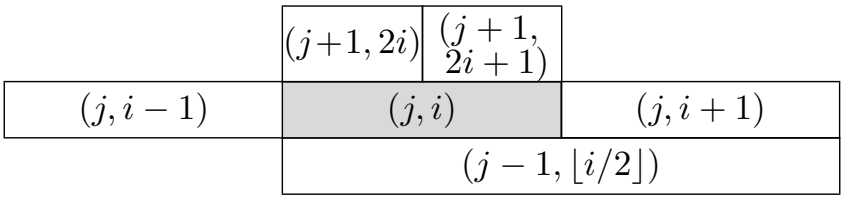

FIG. 2. *Safety zone in wavelet coefficient space around an active coefficient (j, i) in position i and finer $(j+1)$ and coarser scale $(j-1)$, where $\lfloor i/2 \rfloor$ is the floor function, which yields the integer part of its argument*

.

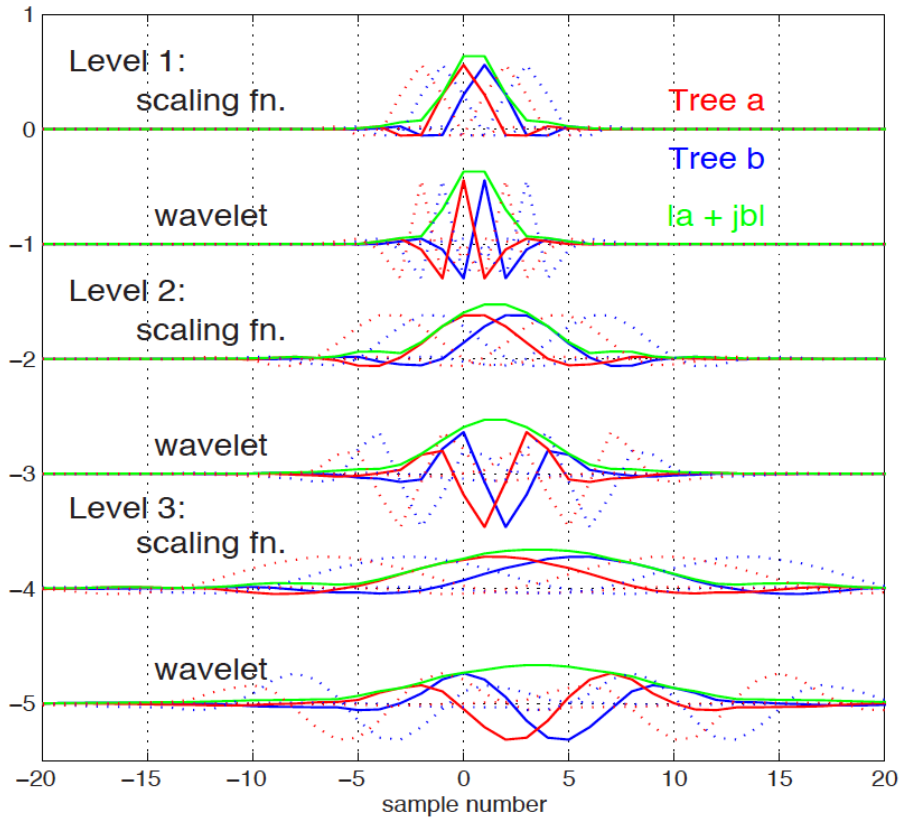

FIG. 3. *Complex wavelet basis functions (Q-shift dual-tree complex-valued wavelet transform) for levels 1 to 3. Basis functions for adjacent sampling points are shown dotted. Courtesy of N. Kingsbury.*

by Kingsbury in 2001 [42], whose wavelets are called Kingslets (the code is available on GitHub; see https://github.com/rjw57/dtcwt). This discrete wavelet transform generates complex-valued coefficients, and a dual tree of wavelet filters is used to obtain their real and imaginary parts. Thus a redundant representation is produced with a redundancy of 2^d, where d once again denotes the dimension of the signal. However, the transform provides approximate shift invariance and directionally selective filters. The classical properties of perfect reconstruction and

computational efficiency are preserved and with good well-balanced frequency responses. Analysis of the shift invariance of the transform can be found in [42], together with an estimation of its accuracy and the design of suitable filters. An example for quarter-sample shift (Q-shift) filters, along with the resulting wavelet basis functions, is presented in Figure 3.

Adding a safety zone as mentioned in step (iv) above, an idea originally introduced in [47], is necessary due to the lack of translational invariance of orthogonal wavelets, but also for local dealiasing. The idea is to keep neighboring coefficients in space and scale and to account for translation of shocks or steep gradients and the generation of finer scale structures. For the complex-valued wavelets, which are translation invariant, no safety zone is required, as shown in [61]. For details and further discussion on possible and more efficient choices of the safety zone we refer the reader to [55].

Finally, let us also mention an interesting link with large eddy simulations (LES) where only the large scales of the flow are computed, while the influence of small scales is modeled [70, 17, 46, 9]. In [68] we pointed out that there is an equivalence between nonlinear wavelet thresholding (using Haar wavelets) and a single step of explicitly discretized nonlinear diffusion used in LES, shown in [49] in the context of nonlinear diffusion filtering for image processing.

4. Numerical experiments discarding one coefficient.

4.1. Numerical setup. In the following we show results to illustrate the properties of the adaptive Galerkin scheme and in particular their ability to introduce energy dissipation into the numerical method, which can be useful for stabilization. For examples we consider first the inviscid 1D Burgers equation using periodic boundary conditions. The initial condition is a simple sine wave given by $u(x, t = 0) = \sin(2\pi x)$ for $x \in \mathbb{T}$. Unless explicitly noted, computations are done with $N = 2048$ collocation points, and the time step Δt is chosen so that $\Delta x/\Delta t = 16$, where $\Delta x = 1/N$ is the grid discretization size. This choice ensures the CFL condition is met [7].

4.2. Application in Fourier basis. The simplest illustration which we develop as a proof of concept is a punctual selection in the Fourier basis. Starting at some time instant t_b and during an entire interval $[t_b, t_e]$, we set to zero the Fourier coefficients corresponding to a given wavenumber k_f after each time step (both positive and negative modes are erased, such that the solution remains real). The projection operator thus becomes time dependent and discontinuous, and we have

$$P_N(t)^{k_f}_{[t_b,t_e]} u(x) = \begin{cases} \sum_{|k|\lesssim N/2, |k|\neq k_f} \widehat{u}_k \, e^{ik\,x} & \text{for} \quad t \in [t_b, t_e], \\ \sum_{|k|\lesssim N/2} \widehat{u}_k \, e^{ik\,x} & \text{elsewhere.} \end{cases} \tag{4.1}$$

The removal of these modes will instantly dissipate energy of the numerical solution, but from there on energy is conserved. And this is still the case after the reintroduction of the coefficients in the projection basis, despite the discontinuity of the projection operator. Indeed, according to (2.19) dissipation is observed as long as $\| [1 - P_h(t^+)] \, u_h(t) \|^2$ is nonzero, but at $t = t_e$ this quantity is null and therefore energy is conserved. We note that since a multistage time marching scheme is employed, it is necessary to reset to zero the removed coefficients after each substage, to ensure they have no effect on the solution.

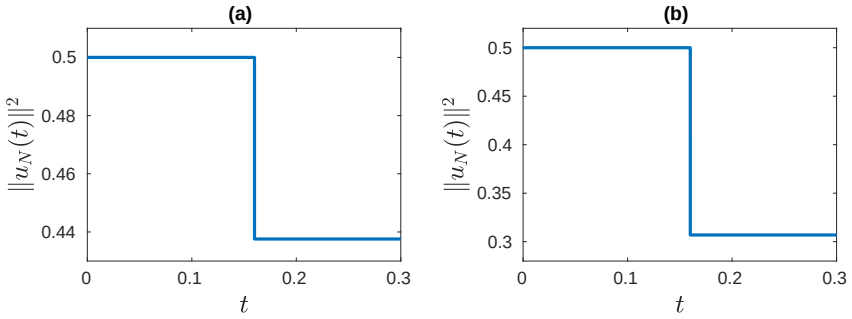

FIG. 4. *Filtering of one mode in (a) Fourier space and (b) in wavelet space for the inviscid 1D Burgers equation. Time evolution of energy. As expected, energy loss is observed.*

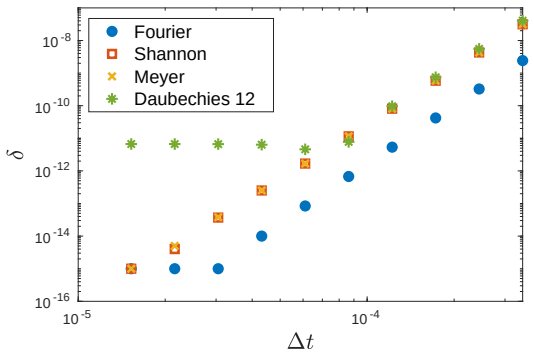

FIG. 5. *Difference between dissipated energy and filtered energy (equation 4.2) as a function of the time step Δt, when a single Fourier mode or wavelet coefficient is filtered. A residual difference remains when Daubechies wavelets are employed.*

We show in Figure 4(a) the time evolution of the energy when the filtering wavenumber is $k_f = 2$. The projection operator changes at $t_b = 0.16$ and is then restored at $t_e = 0.2$. Dissipation is introduced by this change of projection basis and, up to numerical errors, the lost energy amounts to the energy content of the discarded coefficients. This can be seen in Figure 5, where we plot, as a function of the time step Δt, the quantity

$$\delta = (\|u_N(0)\|^2 - \|u_N(t_b)\|^2) - \left\| \left(1 - P_N(t_b^+)_{[t_b,t_e]}^{k_f}\right) u_N(t_b) \right\|^2 , \tag{4.2}$$

which should be zero according to (2.19), since the PDE is energy conserving up to time t_b. One observes that δ indeed converges to zero up to machine precision (of order 10^{-15}) as Δt is decreased. Here, it is interesting to mention that the method developed in [50] employs a punctual periodic filtering in Fourier space to regularize solutions of the inviscid Burgers equation, so the above discussion formalizes the dissipation step used there.

4.3. Application in wavelet basis. To illustrate dissipation through reprojection on a wavelet basis, we extend the previous idea of a punctual selection now to wavelet space. The solution of the Fourier–Galerkin method is decomposed in each time step into a real-valued orthogonal wavelet basis, as in (3.5). One single energy containing coefficient, of scale index j_f and position index i_f, is then set to zero after every time step during some given time interval $[t_b, t_e]$.

The projection operator is once again time dependent and discontinuous and may be written as

(4.3)

$$P_J(t)^{j_f,i_f}_{[t_b,t_e]}u(x) = \begin{cases} \overline{u}_{00} + \sum_{j=0}^{J-1}\sum_{i=0}^{2^j-1} \widetilde{u}_{ji}\psi_{ji}(x)(1-\delta_{jj_f}\delta_{ii_f}) & \text{for} \quad t \in [t_b, t_e], \\ \overline{u}_{00} + \sum_{j=0}^{J-1}\sum_{i=0}^{2^j-1} \widetilde{u}_{ji}\psi_{ji}(x) & \text{elsewhere} \end{cases}$$

for a chosen orthogonal wavelet $\psi_{ji}(x)$.

We show in Figure 4(b) the energy time evolution for the case of projections in the Meyer wavelet basis. The filtered coefficient corresponds to $j_f = 1$ and $i_f = 1$. As before, the filtering happens from time $t_b = 0.16$ to $t_e = 0.2$. Energy is punctually dissipated as of the first change in the projector, but is otherwise conserved. Figure 5 also shows the convergence of the quantity δ from (4.2), now with the projector replaced by (4.3). Similar results are also obtained with projections onto a Shannon wavelet basis.

Interestingly, the same convergence is not observed in Figure 5 when Daubechies wavelets are used. As illustrated in Figure 1, working with Shannon wavelets is actually equivalent to working with the Fourier basis, since it is compactly supported in spectral space, with a sharp cut-off. Combining multiscale Shannon wavelets amounts to covering the spectral space up to some Galerkin cut-off frequency. When projecting with this basis, one is simply damping some existing Fourier coefficients without introducing new wavenumbers. Hence, when going back to the fully dealiased Fourier space, no further energy is lost. The Meyer wavelet is likewise compactly supported in spectral space; however the projection onto Meyer wavelets is only equivalent to a Fourier projection when the number of Fourier modes is increased from N to $3/2N$, which is the case when dealiasing is applied. Therefore, in both cases the dissipated energy indeed corresponds to the energy lost due to the discontinuity of the projection operator. The Daubechies wavelet, on the other hand, is not compactly supported in spectral space. When a projection is made in wavelet space and some coefficient is discarded, this will affect wavenumbers beyond the dealiased ones, which then cease to vanish. After returning to Fourier space, the dealiasing operation will set all these to zero and further energy dissipation occurs. For this reason, the quantity δ shows a residual value as the time step decreases and does not attain machine precision, as seen in Figure 5. In this simulation, Daubechies 12 wavelets were employed and the projector corresponds to (4.3) with $j_f = 0$ and $i_f = 0$. Note that the indices are chosen so that the amount of dissipated energy is comparable in all cases.

This additional energy dissipation can once again be understood as being due to a change in the projector, i.e., going from the wavelet projector removing one coefficient, given in (4.3), to the Fourier projector given in (3.1). In other words, it is the fact that these two projectors do not commute when Daubechies wavelets are used (or any other basis not compactly supported in Fourier space, i.e., within the fully dealiased spectral space) which leads to more dissipation than that introduced by the filtering. This shows that pseudoadaptive simulations, such as those discussed in section 3, must be taken with care, since they may not exactly reproduce what one would get with a fully adaptive scheme in wavelet space. Still, they are valuable tools to predict the solutions behavior in a simpler and faster setup, and we shall apply them to illustrate the introduction of dissipation in conservation laws through an adaptive Galerkin scheme.

5. Application of wavelets to the inviscid Burgers and incompressible Euler equations. In the following section we present in a concise way some results from the literature to illustrate the dissipation properties of adaptive Galerkin methods using CVS denoising. We show some numerical examples for the 1D inviscid Burgers equation, including continuous wavelet analysis and some space-time convergence, and for the incompressible Euler equations in two and three dimensions. For details on the numerical simulations we refer the reader to [61] and [23].

5.1. Continuous wavelet analysis of inviscid 1D Burgers equation. To gain some insight into the formation of the resonance, we perform a continuous wavelet analysis of the Galerkin truncated solutions to the inviscid Burgers equation, as done in [61]. The wavelet representation unfolds the solution in both space and scale in a continuous fashion. It thus allows us to visualize at which wavenumbers and positions the resonances are generated and subsequently propagated.

The continuous wavelet coefficients of the Galerkin-truncated inviscid Burgers equation are calculated as the inner products of the velocity $u(x,t)$ at a given instant t with a set of wavelet functions $\psi_{\ell,x}(x)$ of scales ℓ centered around positions x, i.e.,

$$\widetilde{u}_{\ell,x}(t) \;=\; \int_0^{2\pi} u(x',t)\,\psi^\star_{\ell,x}(x')\,dx', \tag{5.1}$$

where

$$\psi_{\ell,x}(x') = \frac{1}{\sqrt{\ell}}\,\psi\left(\frac{x'-x}{\ell}\right)$$

and $\psi(x) = Ce^{-x^2/\alpha^2}(e^{i\pi x} - e^{\pi^2\alpha^2/4})$, with $\alpha = 4$, C a normalization factor, and $\cdot^\star$ denoting the complex conjugate. This mother wavelet, which is the complex-valued Morlet wavelet [37], has excellent analysis properties [22, 26]. The results, presented in Figure 6, show the logarithm of the modulus of wavelet coefficients at different positions x and scales ℓ (represented by the equivalent wavenumbers $k = \frac{k_\psi}{\ell}$, k_ψ being the centroid wavenumber of the chosen wavelet [22]). The horizontal black line indicates the Galerkin-truncation frequency, and the velocity fields themselves are also shown at the top of each figure for convenience.

Figures 6(a) and 6(b) show, respectively, a harmonic initial condition, here $u_0(x) = \sin(2\pi x)+\sin(4\pi x+0.9)+\sin(6\pi x)$, and how the precursors of the shocks develop. The solution is computed with a truncated Fourier–Galerkin method, described in section 3 using $N = 8192$ modes. Figure 6(c) shows the solution when the first preshock reaches the cut-off scale and becomes a shock, i.e., when nonnegligible energy reaches the scale indicated by the horizontal black line. We observe that the first numerical resonances appear immediately after that and then spread all over space. Note the small time interval between Figures 6(c) and 6(d). Figure 6(e) shows the formation of the bulges around the resonant locations. They stretch until they reach the Galerkin scale and then generate more truncation waves, as shown in Figure 6(f). After that, perturbations at all scales start to spread throughout the solution and even more so when the second shock is formed, as in Fig. 6(g). For much longer time the Burgers solution then becomes very noisy, (Figure 6(h)), on its way towards energy equipartition. Corresponding movies showing the time evolution of the solution and the corresponding wavelet

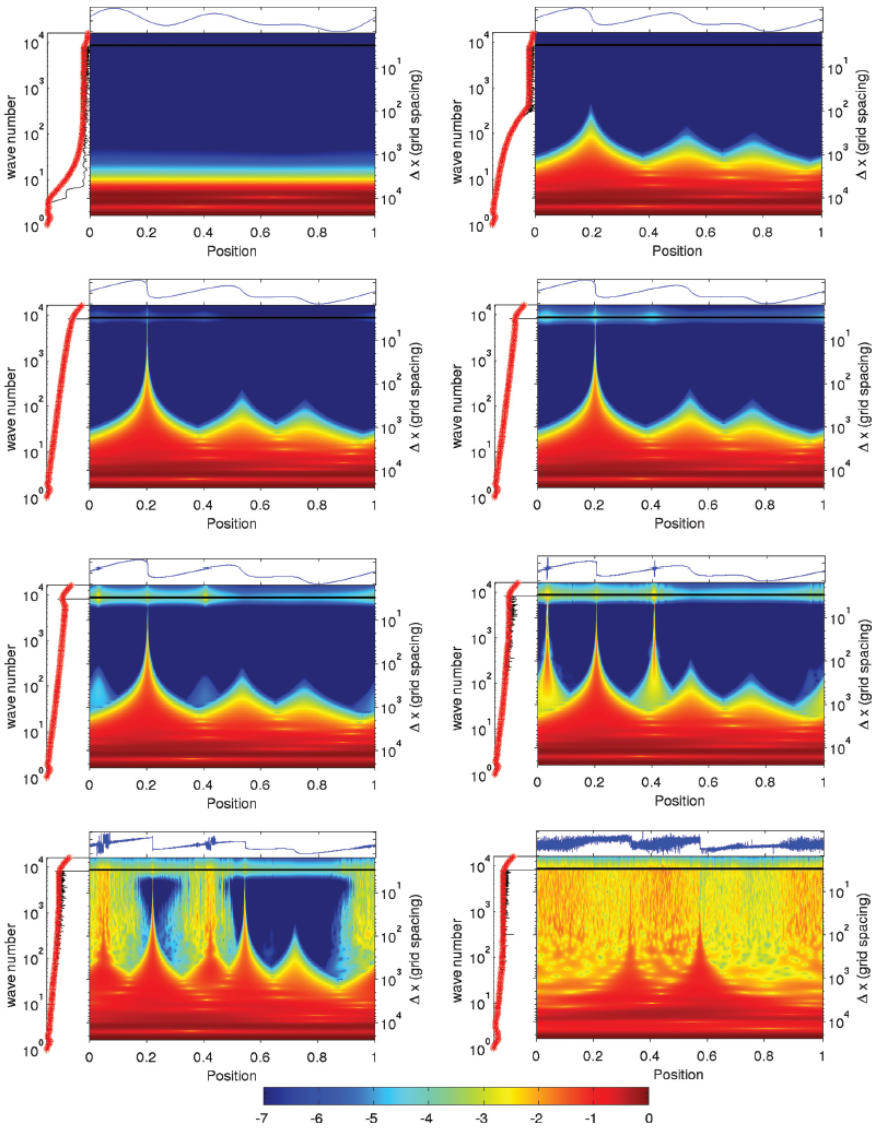

FIG. 6. *Plots of the* $\log_{10}$ *of the moduli of the continuous wavelet coefficients* $\widetilde{u}_{\ell,x}(t)$ *of the Galerkin-truncated solution at times (a)* $t = 0$*, (b)* $t = 0.02749$*, (c)* $t = 0.03505$*, (d)* $t = 0.03538$*, (e)* $t = 0.03648$*, (f)* $t = 0.03998$*, (g)* $t = 0.05897$*, and (h)* $t = 0.19989$*. Each plot shows the solution on the top and below the* $\log_{10}$ *of the modulus of the corresponding continuous wavelet coefficients. The corresponding wavenumber spectrum is plotted vertically on the left. Note that the initial condition here is* $u_0(x) = \sin(2\pi x) + \sin(4\pi x + 0.9) + \sin(6\pi x)$*. Figure reprinted from [61] with permission from the American Physical Society.*

coefficients can be found online*.

*Videos with the time evolution of the continuous wavelet coefficients can be found at http://www.youtube.com/watch?v=WX2YIHGR7LA and http://www.youtube.com/watch?v=j4VfBGgSy30

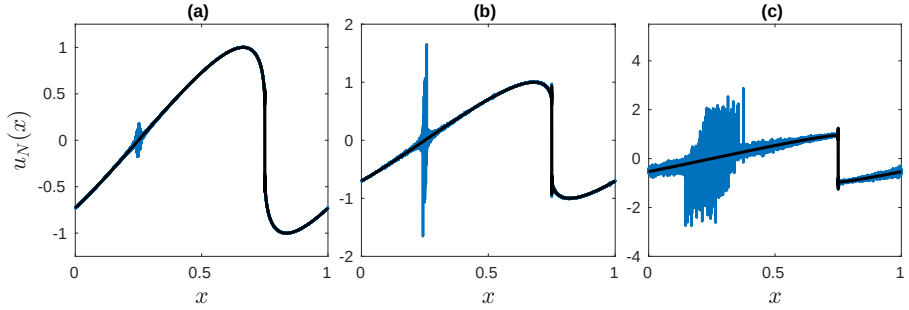

FIG. 7. *CVS denoised Galerkin truncated inviscid Burgers equation using complex-valued wavelets (Kingslets, in black) together with the non-dissipative Galerkin truncated solution (blue) at times* $t = 0.1644$, 0.1793 *and* 0.3. *The solutions are periodically shifted to the right, so that both the resonances and the shocks can be easily seen.*

5.2. Discrete wavelet filtering of inviscid 1D Burgers equation. We consider the inviscid Burgers equation (3.2), discretized with a Fourier pseudospectral method and endowed with CVS filtering, described in section 3, using $N = 16384$ Fourier modes. For the used sinusoidal initial condition $u(x, t = 0) = \sin(2\pi t)$ the time evolution of the reference solution, the so-called entropy solution, can be easily computed with the method of characteristics, separately in each half of the domain. Figure 7 shows the solution of the standard Fourier–Galerkin method, which preserves energy, and the solution obtained with the dynamic Galerkin scheme using CVS filtering with 'Kingslets'. We observe that the oscillations (also called resonances; see [65]), which appear as soon as the shock is formed, are removed using CVS denoising. This is further confirmed in Figure 9 (left), where the oscillations are shown to be completely filtered out and a smooth solution close to the reference solution is obtained.

To assess the filtering performance, we develop a space-time convergence analysis by computing the time integrated relative L^2-distance from the denoised solution u_N to the analytical reference solution u_{ref}. We compute

$$\mathcal{E} = \int_{t_0}^{t_1} \frac{\|u_N(t) - u_{\mathrm{ref}}(t)\|^2}{\|u_{\mathrm{ref}}(t)\|^2} dt \tag{5.2}$$

for different space resolutions while keeping fixed the previous relation between time and space discretization, that is, $\Delta x/\Delta t = 16$. Since the filtering is only relevant after the shock formation, we actually start the analysis from a time right before the shock time $t_s = \inf_x [-1/u'(x, 0)] \approx 0.1592$, i.e., $t_0 = t_s - \Delta t$, and carry on the integration up to $t_1 = 0.3$. Results for complex-valued Kingslets and real-valued Shannon wavelets with and without the safety zone discussed in section 3 are shown in Figure 8. We can observe that CVS with Kingslets is in excellent agreement with the reference solution, showing an $\mathcal{O}(\Delta x)$ convergence rate. Although typically one order of magnitude poorer (an underperformance that we now quantify but which has only been visually verified in [61]), CVS with Shannon wavelets also shows first order convergence towards the reference solution if the safety zone is present. We note that this is the same convergence rate observed with the periodic Fourier filtering of [50]. In comparison to this method, CVS has the disadvantage of being less simply implemented, but offers the attractive feature of compression, with only a very reduced number of degrees of

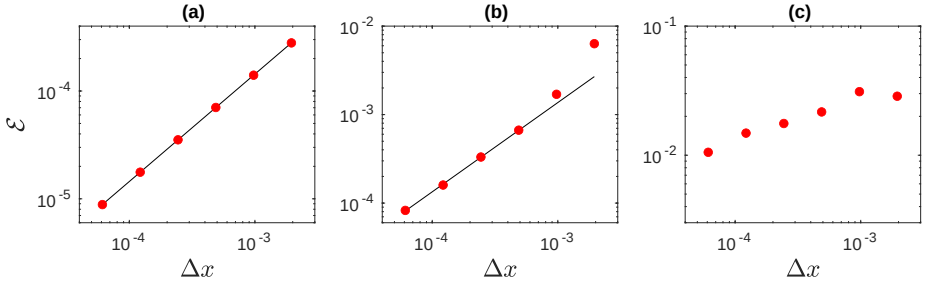

FIG. 8. *Time integrated relative L^2-error (equation 5.2) as a function of space resolution Δx. (a) Kingslets. (b) Shannon wavelet with the safety zone. (c) Shannon wavelet without the safety zone. The straight lines have slope 1.*

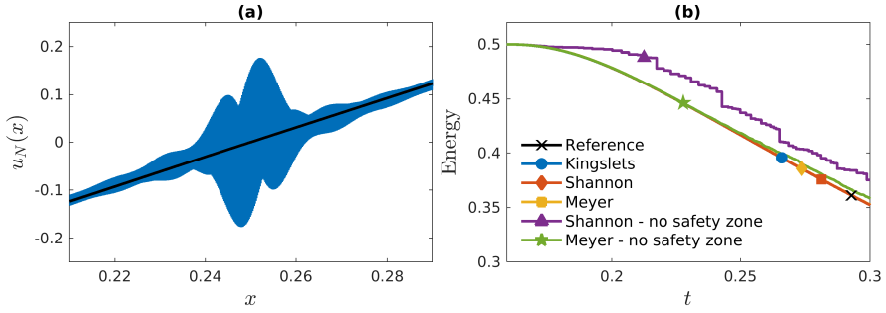

FIG. 9. *(a) Detail of the solution of CVS-denoised Galerkin truncated inviscid Burgers equation using complex-valued wavelets (Kingslets, in black) together with the nondissipative Galerkin truncated solution (blue) at time $t = 0.1644$. Right: Time evolution of the energy $E(t)$ of CVS filtered solutions for different wavelets with and without safety zone together with the analytical result.*

freedom being necessary to reproduce the physical reference solution. Meanwhile, as anticipated in section 3, Figure 8(c) shows that CVS is not able to properly regularize the solution when employing real orthogonal wavelets if a safety zone is not introduced.

The evolution of the energy $E = \frac{1}{2}||u||^2$ shown in Figure 9 (right) further quantifies the dissipation of the adaptive schemes for different real orthogonal wavelets. Once again, in the presence of the safety zone the wavelet adaptation removes sufficient energy, matching thus the analytical energy evolution. However, it is now seen that without the safety zone not enough energy is dissipated and the solution is not properly regularized. For a detailed description of similar simulations and a physical interpretation we refer the reader to [61].

5.3. Discrete wavelet denoising of incompressible 2D Euler equation. To illustrate the effect of dissipation when adapting the basis functions using projectors changing over time we consider the incompressible Euler equations given in (3.4) and discretize them with a classical Fourier–Galerkin scheme. In these pseudoadaptive simulations we apply in each time step CVS denoising. Detailed results can be found in [61] and [23] for the 2D and 2D cases, respectively.

In the 2D case a random initial condition is evolved in time with third order Runge–Kutta time integration using a resolution of $N = 1024^2$ Fourier modes [61]. Visualizations of the Laplacian of the vorticity field $\omega = \nabla \times \boldsymbol{u}$ in the fully

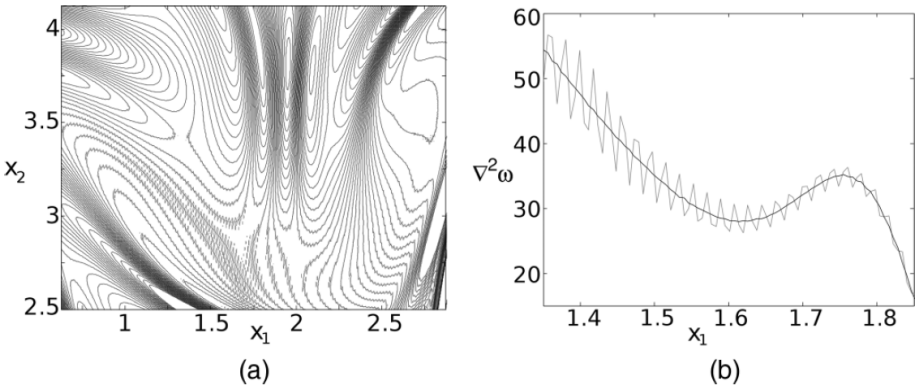

FIG. 10. *Filtering of 2D incompressible Euler using complex-valued wavelets (Kingslets). Left: Contours of the Laplacian of vorticity* $\nabla^2\omega$ *at* $t = 0.71$. *The Galerkin truncated solution is shown in gray, and the CVS solution is given in black. Right: 1D cut of the Laplacian of vorticity for the oscillatory Galerkin truncated solution and the wavelet-filtered smooth solution. Figure reprinted from [61] with permission from the American Physical Society.*

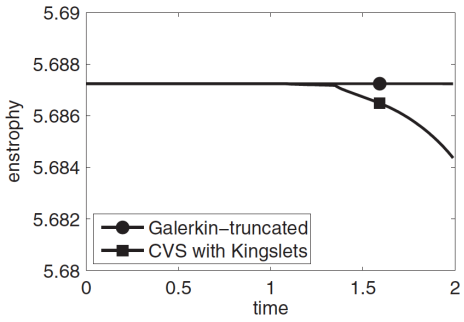

FIG. 11. *Filtering of 2D incompressible Euler using complex-valued wavelets (Kingslets). Evolution of enstrophy* $1/2||\omega||_2^2$ *for the Galerkin truncated case and the adaptive wavelet denoised case using Kingslets. Figure reprinted from [61] with permission from the American Physical Society.*

developed nonlinear regime are shown in Figure 10 (left). For the Galerkin truncated solution we find numerical resonances on the isolines of $\nabla^2\omega = (\partial_{xx} + \partial_{yy})\,\omega$ (a small scale quantity, which is sensitive to oscillations), while the regularized solution using complex-valued wavelets with CVS filtering yields a smooth solution. A 1D cut in Figure 10 (right) illustrates that in the CVS solution the oscillations have been indeed removed. Time evolution of enstrophy, defined as $\frac{1}{2}||\omega||_2^2$, shows that in contrast to the Galerkin truncated simulation, the CVS computation is dissipative, with enstrophy departing from the one of the conservative Galerkin truncated case and decaying for times larger than 1.4. For more details including a physical interpretation we refer the reader to [61].

5.4. Discrete wavelet denoising of incompressible 3D Euler equation. The three-dimensional Fourier–Galerkin computations of incompressible Euler have been performed at resolution $N = 512^3$ in a periodic cubic domain with a fourth order Runge–Kutta scheme for time integration [23]. A statistically

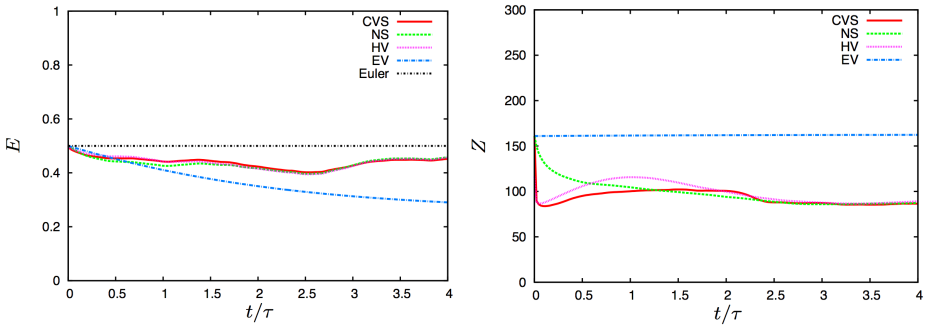

FIG. 12. *Energy (left) and enstrophy (right) evolution for 3D incompressible Euler using for Galerkin-truncated Euler (Euler), wavelet denoised Euler (CVS), and Navier-Stokes (NS). HV and EV stand for hyperviscous regularization and Euler–Voigt, respectively, which are not discussed here. Figure reprinted from [23] with permission from the American Physical Society.*

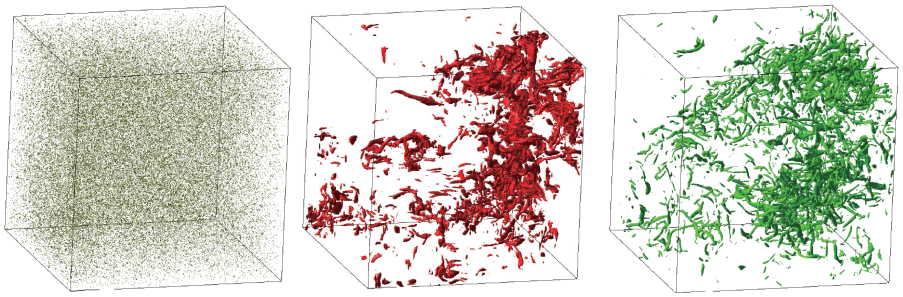

FIG. 13. *Vorticity isosurfaces, $|\boldsymbol{\omega}| = M + 4\sigma$ (where M is the mean value and σ the standard deviation of the modulus of vorticity of Navier–Stokes) for 3D incompressible Euler using Galerkin-truncated Euler (Euler, left), wavelet filtered Euler (CVS, center) and Navier–Stokes (NS, right) at time $t/\tau = 3.4$, where τ is the initial eddy turn over time. Figure reprinted from [23] with permission from the American Physical Society.*

stationary flow of fully developed homogeneous isotropic turbulence obtained by DNS is used as initial condition. For CVS filtering, Coiflet 12 wavelets [14] were used. Note that the wavelet decomposition and subsequent filtering have been applied to the vorticity $\boldsymbol{\omega} = \nabla \times \boldsymbol{u}$ (and not to the velocity $\boldsymbol{u}$) in each time step, and subsequently the filtered velocity has been computed by applying the Biot–Savart operator $(\nabla\times)^{-1}$ in Fourier space.

The time evolution of the energy, $\frac{1}{2}||\boldsymbol{u}||_2^2$, and enstrophy, $\frac{1}{2}||\boldsymbol{\omega}||_2^2$, in Figure 12 first shows that the Galerkin-truncated Euler computation preserves energy and that enstrophy grows rapidly in time due to the absence of regularization. For CVS we can observe that energy is dissipated, similar to what is observed for Navier–Stokes and that enstrophy also exhibits a similar evolution to that as Navier–Stokes and does not grow rapidly.

Visualizations of intense vorticity structures in Figure 13 for CVS and Navier–Stokes show their similar tube-like character, while the Galerkin truncated Euler solution is similar to Gaussian white noise without the presence of coherent structures. For details including a physical interpretation of the results we refer the reader to [23].

6. Conclusion. We presented a mathematical framework for analyzing adaptive Galerkin discretizations of evolutionary PDEs. The concept of weak formulations of countable ODEs with nonsmooth right-hand side in Banach spaces was used. We showed that changing the set of active basis functions, which implies that the projection operator is nondifferentiable in time, can introduce energy dissipation. This feature is of crucial interest when using adaptive schemes for time-dependent equations and yields a mathematical explanation for their regularizing properties due to dissipation. Existence and uniqueness of the weak formulation of the adaptive Galerkin solution were likewise proven.

Numerical experiments illustrated the above results for the inviscid Burgers equation in one dimension and the incompressible Euler equations in two and three space dimensions. To this end we performed simulations with the classical Fourier–Galerkin discretization and tested the influence of wavelet thresholding for denoising, comparing different choices of wavelets. The results showed that adaptive wavelet-based regularization (i.e., filtering out the weak wavelet coefficients) of Galerkin schemes introduce dissipation. The latter can be used for reducing the computational cost in fully adaptive computations. Moreover, for the 1D Burgers equation we showed convergence towards the entropy solution. For the 2D and 3D Euler equations we found that numerical resonances present in the Galerkin-truncated case are removed and energy is dissipated. However, for 2D and 3D Euler in general no exact reference solutions are available and further analyses are necessary, which are left for future work.

The main perspective of this work is the further study of adaptive Galerkin discretization, in particular wavelet-based schemes, with possible applications to the understanding of turbulent flows and nonlinear hyperbolic conservation laws.

Acknowledgment. The authors would like to thank Greg Hammett for a discussion which strongly motivated this work.

REFERENCES

[1] A. Azzalini, M. Farge and K. Schneider. *Nonlinear wavelet thresholding: A recursive method to determine the optimal denoising threshold.* Appl. Comput. Harmon. Anal., 18(2), 177-185, 2005.

[2] D. Banerjee and S.S. Ray. *Transition from dissipative to conservative dynamics in equations of hydrodynamics.* Phys. Rev. E, 90(4), 041001, 2014.

[3] C. Bardos, J. S. Linshiz, and E. S. Titi. *Global regularity for a Birkhoff-Rott-α approximation of the dynamics of vortex sheets of the 2d Euler equations.* Phys. D, 237, 1905–1911, 2008.

[4] C. Bardos and E. Tadmor. *Stability and spectral convergence of Fourier method for nonlinear problems: on the shortcomings of the 2/3 de-aliasing method.* Numer. Math., 129(4), 749-782, 2013.

[5] C. Basdevant, B. Legras, R. Sadourny, and M. Béland. *A study of barotropic model flows: intermittency, waves and predictability.* J. Atmospher. Sci., 38, 2305–2326, 1981.

[6] A. Brandt. *Multi-level adaptive solutions to boundary-value problems*, Math. Comp., 31, 333–390, 1977.

[7] C. Canuto, A. Quarteroni, M. Y. Hussaini, and T. A. Zang. *Spectral methods in fluid dynamics.* Springer-Verlag, 1988.

[8] C. Cichowlas, P. Bonaïti, F. Debbasch, and M. Brachet. *Effective Dissipation and Turbulence in Spectrally Truncated Euler Flows.* Phys. Rev. Lett. 95, 264502, 2005.

[9] R.A. Clark, J.H Ferziger and W.C. Reynolds. *Evaluation of subgrid-scale models using an accurately simulated turbulent flow.* J. Fluid Mech., 91(1), 1-16, 1979.

[10] A. Cohen. *Wavelet methods in numerical analysis,* Handbook Numer. Anal. 7, Eds. P.G. Ciarlet & J.L. Lions, Elsevier, 2000.

[11] P. Constantin, W. E and E.S. Titi. *Onsager's conjecture on the energy conservation for*

solutions of Euler's equation. Commun. Math. Phys., 165(1), 207-209, 1994.
[12] W. Dahmen, A. Kunoth and K. Urban. *A wavelet Galerkin method for the Stokes equations.* Computing, 56, 259–301, 1996.
[13] W. Dahmen, K. Urban and J. Vorloeper. *Adaptive wavelet methods: basic concepts and applications to the Stokes problem.* In Wavelet Analysis, ed. DX Zhou, 39–80, World Scientific Singapore, 2002.
[14] I. Daubechies. *Ten lectures on wavelets.* SIAM, Philadelphia, 1992.
[15] C. De Lellis and L. Székelyhidi Jr. *Dissipative Euler flows and Onsager's conjecture.* J. European Math. Soc., 16(7), 1467-1505, 2014.
[16] K. Deimling. *Ordinary differential equations in Banach spaces.* Springer, 1977.
[17] J.W. Deardorff. *A numerical study of three-dimensional turbulent channel flow at large Reynolds numbers.* J. Fluid Mech., 41(2), 453-480, 1970.
[18] P.C. Di Leoni, P.D. Mininni and M.E. Brachet. *Dynamics of partially thermalized solutions of the Burgers equation.* Phys. Rev. Fluids, 3(1), 014603, 2018
[19] D.L. Donoho and I.M. Johnstone. *Ideal spatial adaptation by wavelet shrinkage.* Biometrika, 81(3), 425-455, 1994.
[20] T. Engels, K. Schneider, J. Reiss and M. Farge. *A wavelet adaptive method for multiscale simulation of turbulent flows in flying insects.* Commun. Comput. Phys., 30(4), 1118-1149, 2021.
[21] A.C. Ewing. *Review of The Scientific Outlook, by Bertrand Russell.(London: George Allen & Unwin Ltd. 1931).* Philosophy, 7, 233-235, 1932.
[22] M. Farge. *Wavelet transforms and their applications to turbulence.* Annu. Rev. Fluid Mech., 24(1), 395-458, 1992.
[23] M. Farge, N. Okamoto, K. Schneider and K. Yoshimatsu. *Wavelet-based regularization of the Galerkin truncated three-dimensional incompressible Euler flows.* Phys. Rev. E, 96, 063119, 2017.
[24] M. Farge, G. Pellegrino and K. Schneider. *Coherent vortex extraction in 3D turbulent flows using orthogonal wavelets.* Phys. Rev. Lett., 87(5), 054501, 2001.
[25] M. Farge and K. Schneider. *Coherent vortex simulation (CVS), a semi-deterministic turbulence model using wavelets. Flow Turb. Combust.*, 66(4), 393-426, 2001.
[26] M. Farge and K. Schneider. *Wavelet transforms and their applications to MHD and plasma turbulence: a review.* J. Plasma Phys., 81(6), 435810602, 2015.
[27] M. Farge, K. Schneider and N. Kevlahan. *Non-Gaussianity and coherent vortex simulation for two-dimensional turbulence using an adaptive orthogonal wavelet basis.* Phys. Fluids, 11(8), 2187–2201, 1999.
[28] M. Farge, K. Schneider, G. Pellegrino, A.A. Wray and R.S. Rogallo. *Coherent vortex extraction in three-dimensional homogeneous turbulence: Comparison between CVS-wavelet and POD-Fourier decompositions.* Phys. Fluids, 15(10), 2886-2896, 2003.
[29] A.F. Filippov. *Differential equations with discontinuous right hand sides.* Math. Appl. (Soviet Ser.) 18, Springer Science & Business Media, 2013.
[30] U. Frisch, S. Kurien, R. Pandit, W. Pauls, S.S. Ray, A. Wirth, and J.Z. Zhu, *Hyperviscosity, Galerkin truncation, and bottlenecks in turbulence.* Phys. Rev. Lett., 101(14), 144501, 2008.
[31] U. Frisch, S.S. Ray, G. Sahoo, D. Banerjee, and R. Pandit. *Real-space manifestations of bottlenecks in turbulence spectra.* Phys. Rev. Lett., 110(6), 064501, 2013.
[32] J. Fröhlich and K. Schneider. *An adaptive wavelet Galerkin algorithm for one- and two-dimensional flame computations.* European J. Mech. B Fluids, 13, 439-471, 1994.
[33] J. Fröhlich and K. Schneider. *Numerical simulation of decaying turbulence in an adaptive wavelet basis.* Appl. Comput. Harm. Anal., 3(4), 393-397, 1996.
[34] J. Fröhlich and K. Schneider. *An adaptive wavelet–vaguelette algorithm for the solution of PDEs.* J. Comput. Phys., 130(2), 174-190, 1997.
[35] J. Fröhlich and K. Schneider. *Computation of decaying turbulence in an adaptive wavelet basis.* Phys. D, 134(3), 337-361, 1999.
[36] D. Gottlieb and J. S. Hesthaven. *Spectral methods for hyperbolic problems.* J. Comput. Appl. Math., 128, 83–131, 2001.
[37] A. Grossmann and J. Morlet. *Decomposition of Hardy functions into square integrable wavelets of constant shape.* SIAM J. Math. Anal., 15(4), 723-736, 1984.
[38] A. Harten. *High resolution schemes for hyperbolic conservation laws.* J. Comput. Phys., 49(3), 357–393, 1983.
[39] T.Y. Hou and P.D. Lax. *Dispersive approximations in fluid dynamics.* Commun. Pure Appl. Math., 44(1), 1–40, 1991.
[40] T. Ishihara, T. Gotoh and Y. Kaneda. *Study of high–Reynolds number isotropic turbulence by direct numerical simulation.* Annu. Rev. Fluid Mech., 41, 165-180, 2009.

[41] B. Khouider and E. S. Titi. *An inviscid regularization for the surface quasi-geostrophic equation.* Commun. Pure Appl. Math., 61(10), 1331–1346, 2008.
[42] N. Kingsbury. *Complex wavelets for shift invariant analysis and filtering of signals.* Appl. Comput. Harm. Anal., 10(3), 234–253, 2001.
[43] S.S.V. Kolluru, P. Sharma and R. Pandit. *Insights from a pseudospectral study of a potentially singular solution of the three-dimensional axisymmetric incompressible Euler equation.* Phys. Rev. E, 105(6), 065107, 2022.
[44] R.H. Kraichnan. *Inertial ranges in two-dimensional turbulence.* Phys. Fluids, 10(7), 1417-1423, 1967.
[45] T.D. Lee. *On some statistical properties of hydrodynamical and magneto-hydrodynamical fields.* Quart. Appl. Math., 10(1), 69-74, 1952.
[46] A. Leonard. *Energy cascade in large-eddy simulations of turbulent fluid flows.* in Advances in Geophysics, Vol. 18, Elsevier, 237-248, 1975.
[47] J. Liandrat and P. Tchamitchian. *Resolution of the 1D regularized Burgers equation using a spatial wavelet approximation.* Report 187480, NASA, 1990.
[48] A. Majda and I. Timofeyev, *Remarkable Statistical Behavior for Truncated Burgers–Hopf Dynamics.* Proc. Natl. Acad. Sci. USA, 97(23), 12413-12417, 2000.
[49] P. Mrázek, J. Weickert and G. Steidl. *Correspondences between wavelet shrinkage and nonlinear diffusion.* In Scale-Space 2003, Lecture Notes in Comput. Sci. 2695, eds. L. D. Griffin and M. Lillholm, Springer, Berlin, 101–116, 2003.
[50] S.D. Murugan, U. Frisch, S. Nazarenko, N. Besse and S.S. Ray. *Suppressing thermalization and constructing weak solutions in truncated inviscid equations of hydrodynamics: Lessons from the Burgers equation.* Phys. Rev. Res., 2(3), 033202, 2020.
[51] S.D. Murugan and S.S. Ray. *On the thermalization of the three-dimensional, incompressible, Galerkin-truncated Euler equation.* preprint, https://arxiv.org/abs/2209.05046, 2022.
[52] R. Nguyen van yen, M. Farge, D. Kolomenskiy, K. Schneider and N. Kingsbury. *Wavelets meet Burgulence: CVS-filtered Burgers equation.* Phys. D, 237(14), 2151-2157, 2008.
[53] R. Nguyen van yen, M. Farge and K. Schneider. *Wavelet regularization of a Fourier–Galerkin method for solving the 2D incompressible Euler equations.* ESAIM Proc., 29, 89-107, 2009.
[54] N. Okamoto, K. Yoshimatsu, K. Schneider, M. Farge and Y. Kaneda. *Coherent vortices in high resolution direct numerical simulation of homogeneous isotropic turbulence: A wavelet viewpoint.* Phys. Fluids, 19, 115109, 1-13, 2007.
[55] N. Okamoto, K. Yoshimatsu, K. Schneider, M. Farge and Y. Kaneda. *Coherent vortex simulation of three-dimensional decaying homogeneous isotropic turbulence.* Multiscale Model. Simul., 9(3), 1144-1161, 2011.
[56] L. Onsager. *Statistical hydrodynamics.* Il Nuovo Cimento (1943-1954), 6 (Suppl 2), 279-287, 1949.
[57] P. Orlandi. *Fluid Flow Phenomena: A Numerical Toolkit.* Springer, 2000.
[58] S. Osher and F. Solomon. *Upwind difference schemes for hyperbolic systems of conservation laws.* Math. Comput., 38(158), 339–374, 1982.
[59] S.G. Pandit and S.G. Deo. *Differential equations involving impulses.* Lecture Notes in Math. 954, Springer, 1982.
[60] G.S. Patterson Jr and S.A. Orszag. *Spectral calculations of isotropic turbulence: Efficient removal of aliasing interactions.* Phys. Fluids, 14(11), 2538-2541, 1971.
[61] R. M. Pereira, R. Nguyen van yen, M. Farge and K. Schneider. *Wavelet methods to eliminate resonances in the Galerkin-truncated Burgers and Euler equations.* Phys. Rev. E, 87, 033017, 2013.
[62] R.M. Pereira, N. Nguyen van yen, K. Schneider and M. Farge. *Adaptive solution of initial value problems by a dynamical Galerkin scheme.* Multiscale Model. Simul., 20(3), 1147-1166, 2022.
[63] R. Peyret. *Spectral methods for incompressible viscous flow.* Appl. Math. Sci. 148, Springer, New York, 2002.
[64] C. Rampf, U. Frisch and O. Hahn. *Eye of the tyger: Early-time resonances and singularities in the inviscid Burgers equation.* Phys. Rev. Fluids, 7(10), 104610, 2022.
[65] S. S. Ray, U. Frisch, S. Nazarenko, and T. Matsumuto. *Resonance phenomenon for the Galerkin-truncated Burgers and Euler equations.* Phys. Rev. E, 84, 016301, 2011.
[66] K. Schneider, M. Farge, G. Pellegrino, and M. Rogers. *Coherent vortex simulation of 3D turbulent mixing layers using orthogonal wavelets.* J. Fluid Mech., 534, 39-66, 2005.
[67] K. Schneider and O. Vasilyev. *Wavelet methods in computational fluid dynamics.* Annu. Rev. Fluid Mech., 42, 473-503, 2010.
[68] K. Schneider, J. Ziuber, M. Farge and A. Azzalini. *Coherent vortex extraction and simu-*

lation of 2D isotropic turbulence. J. Turb., 7, N44, 2006.
[69] S. Schwabik. *Generalized ordinary differential equations* Ser. Real Anal. 5, World Scientific, Singapore, 1992.
[70] J. Smagorinsky. *General circulation experiments with the primitive equations: I. The basic experiment.* Month. Weather Rev., 91(3), 99-164, 1963.
[71] P. K. Sweby. *High resolution schemes using flux limiters for hyperbolic conservation laws.* SIAM J. Numer. Anal., 21(5), 995–1011, 1984.
[72] E. Tadmor. *Convergence of spectral methods for nonlinear conservation laws.* SIAM J. Numer. Anal., 26(1), 30–44, 1989.
[73] M. Vergassola, B. Dubrulle, U. Frisch and A. Noullez. *Burgers' equation, devil's staircases and the mass distribution for large-scale structures.* Astronomy Astrophys., 289, 325–356, 1994.
[74] P.K. Yeung and K. Ravikumar. *Advancing understanding of turbulence through extreme-scale computation: Intermittency and simulations at large problem sizes.* Phys. Rev. Fluids, 5(11), 110517, 2020.